Emission engineering in germanium nanoresonators

M. Celebrano, M. Baselli, M. Bollani, J. Frigerio, A. Bahgat Shehata, A. Della Frera, A. Tosi, A. Farina, F. Pezzoli, J. Osmond, X. Wu, B. Hecht, R. Sordan, D. Chrastina, G. Isella, L. Duò, M. Finazzi, P. Biagioni

SUPPORTING INFORMATION

1) X-ray diffraction strain analysis of the Ge sample

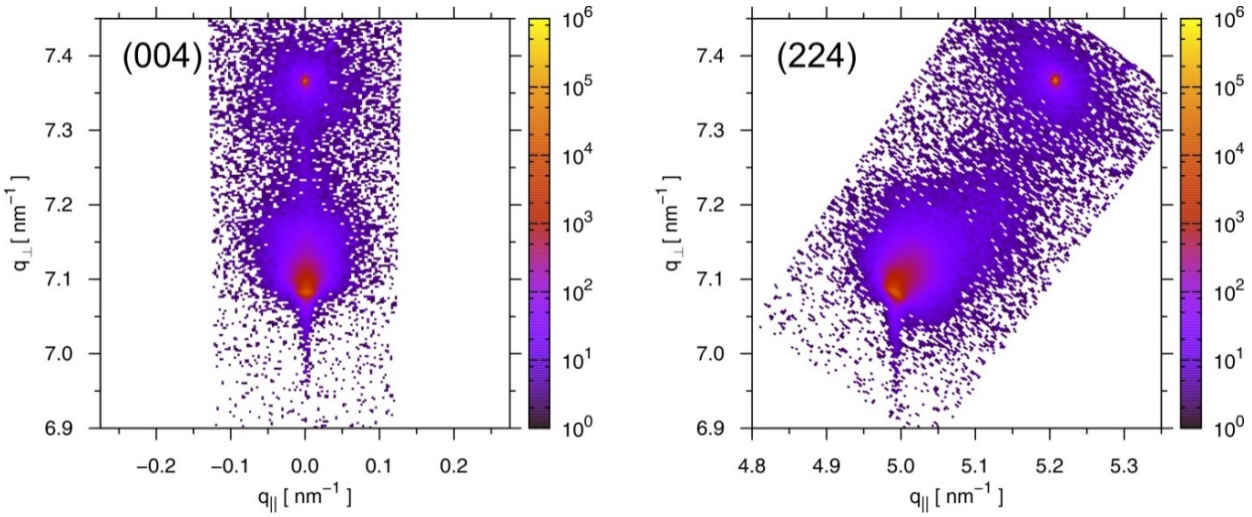

Figure S1 Reciprocal space maps (RSMs) around the (004) (left) and (224) (right) Bragg peaks. The Si substrate peak is visible at $q_\perp = 4/a_{Si} = 7.365$ nm^{-1} in both RSMs, with the Ge peak visible at $q_\perp \cong 7.083$ nm^{-1}. In the (004) RSM the peaks are aligned at $q_\perp \cong 0$ nm^{-1}, indicating that the Ge layer is not tilted with respect to the Si substrate. The (224) RSM shows instead that there is slight tensile strain of the Ge layer since the $q_\parallel/q_\perp$ ratio for the peak is slightly less than $\sqrt{2}$. The presence of intensity in the $q_\perp$ region of 7.1-7.2 nm^{-1} indicates intermixing of Ge and Si during the annealing process.

The lattice parameters of the epitaxial Ge layer were measured by high-resolution x-ray diffraction (HR-XRD), using a PANalytical PRO-MRD diffractometer equipped with a hybrid 2-bounce Ge channel-cut monochromator and mirror on the incidence beam and a 3-bounce analyzer crystal in front of the proportional x-ray point detector. Reciprocal space maps (RSMs) were obtained around

the (004) and (224) Bragg peaks, as shown in Fig. S1. In terms of the x-ray incidence angle ω and the scattering angle 2θ, the components of the scattering vector **q** are defined by [S1]

$$q_{\parallel} = \frac{2}{\lambda}\sin(\theta)\sin(\theta - \omega)$$
$$q_{\perp} = \frac{2}{\lambda}\sin(\theta)\cos(\theta - \omega)$$

with λ = 0.154 nm as the wavelength of Cu $K_{\alpha 1}$ radiation [S2]. The acquisition of two maps at different (*hkl*) allows the tilt, Ge content, and strain state of a $Si_{1-x}Ge_x$ alloy epitaxially deposited on a Si substrate to be determined once the relationship between lattice parameter and Ge content is known [S3]. In this case a Ge content of about 99.4% was found (a small Si content may be present even in nominally pure Ge alloys grown by low-energy plasma-enhanced chemical vapor deposition, due to diffusion from the substrate or the memory effect of the growth chamber) with in-plane tensile strain of $\varepsilon_{\parallel} = 0.22 \pm 0.01\%$. Tensile strain is induced during the annealing procedure due to the different thermal expansion coefficients of Si and Ge [S4] and is not present in unannealed samples. Annealing also leads to some intermixing of Ge and Si, as can be seen from the intensity present at $q_{\perp}$ values slightly larger than the Ge peak itself.

2) FDFD and FDTD simulations

For the two-dimensional FDFD and the three-dimensional FDTD simulations, a spatial mesh of 3 nm is used for the region surrounding the waveguide resonator. The simulation volume is 3 μm wide and perfectly-matched layers are used for the boundary conditions. The dielectric constant of Ge measured by ellipsometry (see next section below) is in good agreement with values from the literature [S5], although we have a large uncertainty in the evaluation of the imaginary part at 1550 nm wavelength from the fitting of the ellipsometric data. Such an uncertainty, however, does not significantly influence the simulation results for the nanoresonators, where losses at 1550 nm are dominated by the low reflectivity at the waveguide end facets.

3) Ellipsometric characterization and emission spectrum of the Ge sample

Ellipsometry measurements on the substrate used for fabrication were performed on a SOPRA GES-5E rotating polarizer ellipsometer in reflection mode and in the photon energy range of 0.72 to 5 eV at the incidence angle of 77º at room temperature. The fitting model used to deduce the optical constants of Ge/Si(100) is based on standard critical point model [S6]. The resulting dielectric constant is shown in Fig. S2 below. Note that the direct bandgap cannot be directly observed in the ellipsometric data because this optical transition is far too weak to generate a significant discontinuity in the dielectric response. This stems from the fact that the absorption coefficient of Ge material is dominated, below the direct band energy, by indirect transitions. When direct transitions come into play, there is an additional contribution to the absorption coefficient depending on the joint density of electron states, which has a van Hove singularity at the direct gap. This means that only the energy derivative of the absorption coefficient is in principle discontinuous.

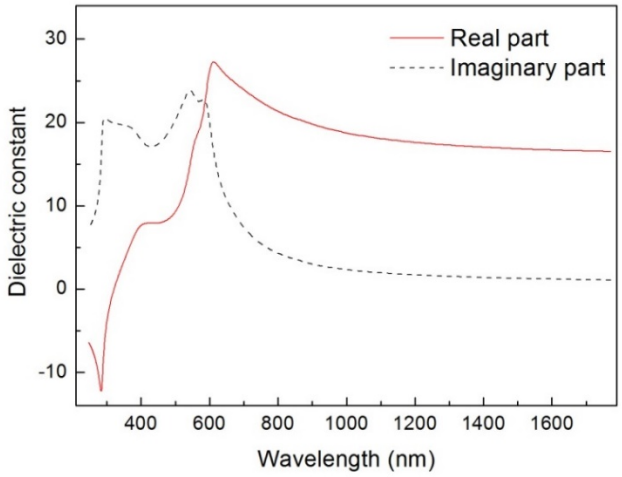

Figure S2 Dielectric constant of the Ge thin film used for the fabrication of the nanoresonators, as obtained from the fitting of the ellipsometric data.

In order to unambiguously prove that the collected light at 1550 nm in the confocal emission maps is the result of radiative recombination across the direct gap of Ge, we acquired room temperature emission spectra from the same continuous Ge film that was used for nanofabrication, exploiting a cooled IR-extended InGaAs detector and an excitation wavelength of 458 nm of an Ar^+ laser. Figure S3 clearly shows the two emission peaks related to direct-gap and indirect-gap recombination, confirming that the light collected at 1550 nm can be almost fully attributed to direct-gap emission. The spectral position of the direct-gap emission is also in fair agreement with previous published results for similar levels of strain and doping [S7].

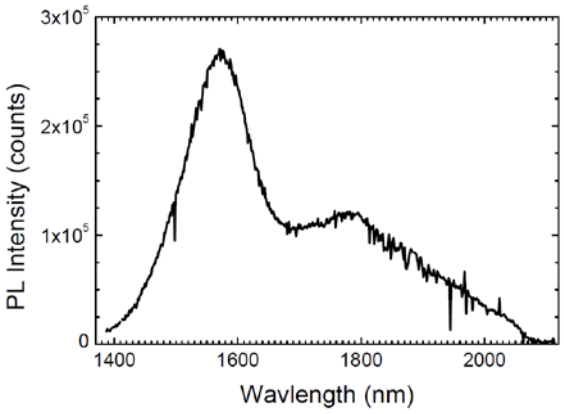

Figure S3 IR-extended emission spectrum from a continuous unpatterned Ge film.

4) FIB milling procedure

Focused ion-beam milling was performed on a FEI Helios NanoLab 600 Dual Beam machine, with 9.7 pA ion beam current and 30 kV acceleration voltage. The milling procedure consists of two steps, as shown in Fig. S4(a). While the first step removes most of the Ge material surrounding the resonator, the second and shorter step defines the final shape of the resonator. Structures milled out of a Ge film with and without silicon oxide layer on top are shown in Figs. S4(b) and S4(c), respectively. It is seen that without the hard silicon oxide layer the top of the resonator is hardly controlled – the edges are not sharp and the top surface is also rougher. This reveals the special material property of Ge against FIB milling, and might also be influenced by the very different sticking coefficient of Ge clusters on Ge or on SiO_x surfaces [S8].

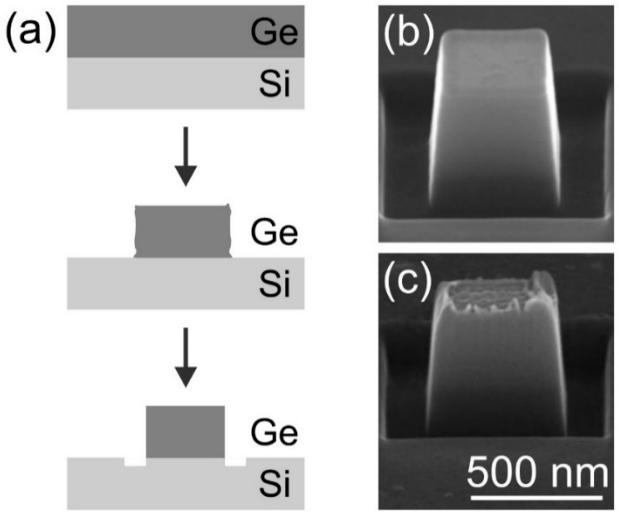

Figure S4 (a) Sketch of the FIB milling sequence; (b) representative image of a nanoresonator obtained with the top SiO_x protective layer; (c) representative image of a nanoresonator obtained without the SiO_x protective layer.

5) Experimental confocal setup

The confocal setup used for the investigation is sketched in Fig. S5(a). The free-space coupled detector is a highly optimized, Peltier-cooled InGaAs/InP single-photon avalanche diode (SPAD) that operates in gated-mode [S9]. The detector is cooled at 230 K and biased 4 V above the breakdown level, in order to have high single-photon detection efficiency [about 26% at 1550 nm, see Fig. S5(b)] and dark count rate less than 10^4 counts per second [S10]. The gate-ON time was set to 40 ns and the gate repetition frequency was 4 MHz, but thanks to the fast active quenching and a hold-off of 40 µs after each avalanche, afterpulsing effect is limited, thus allowing to have low distortion in the acquired signals.

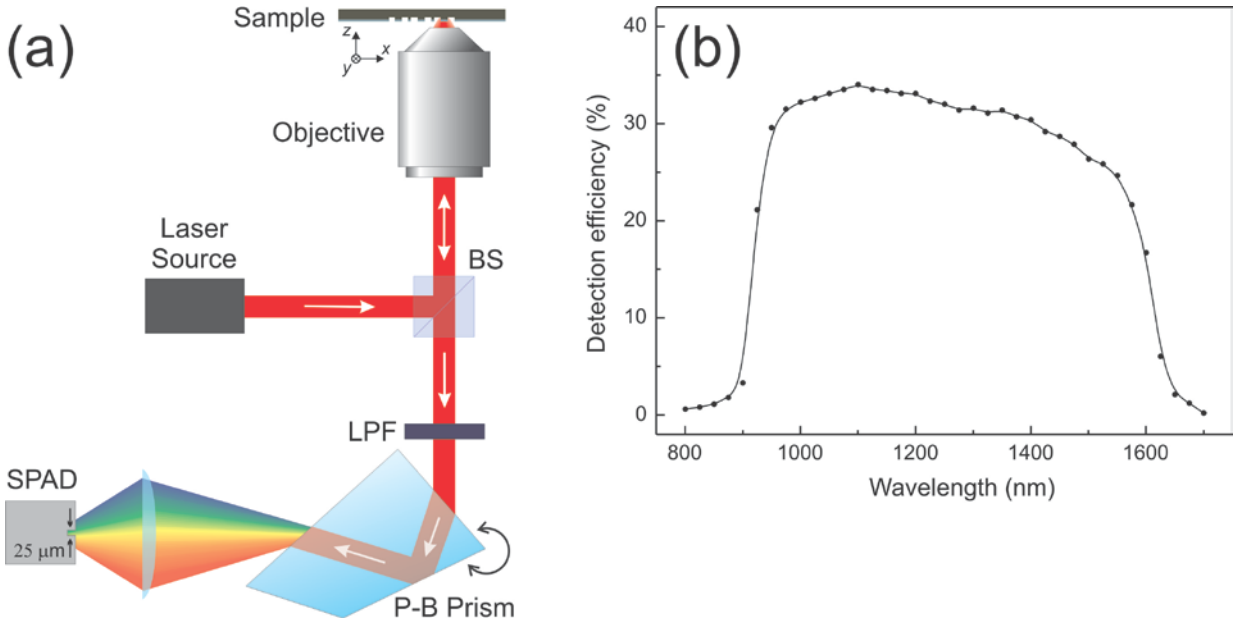

Figure S5 (a) Sketch of the confocal microscope setup (BS, beam splitter; LPF, long-pass filter; P-B prism, Pellin-Broca prism); (b) experimentally-measured detection efficiency of the InGaAs/InP detector.

6) Mode mapping and end-facet reflectivity in Ge-on-Si waveguides

We analyzed the modes sustained by the Ge waveguide for different waveguide cross sections by FDFD simulations. Representative results are shown in Fig. S6. While for lateral dimensions below 300 nm cut-off conditions are reached, for a cross section of about 300×300 nm^2 one quasi-TE and one quasi-TM mode are found, although the field confinement inside the Ge material is still not optimal, as can be seen from the intensity maps in Fig. S6. The field confinement improves for a section of about 400×400 nm^2, which is similar to the one used in our experiments and where again only the lowest-order quasi-TE and quasi-TM modes are supported. For larger sections of about 500×500 nm^2 higher-order modes appear, whose TE/TM character is less well-defined.

Moreover, in order to evaluate the end-facet reflectivity of the actual nanoresonator geometries used in the experiment, we ran FDTD simulations of a semi-infinite truncated waveguide and analyzed the resulting standing-wave by numerical fitting [S11], obtaining an end-facet reflectivity of the order of 68%. A representative map for the standing wave generated by reflection of the quasi-TM mode is shown in Fig. S7, together with the resulting fitting. It can be seen that the intensity profile for the standing wave portion closer to the end facet suffers from additional interference modulations, which we tentatively attribute to light back-scattered by the facet and propagating in air. For this reason, we use only a portion of the standing wave pattern for fitting.

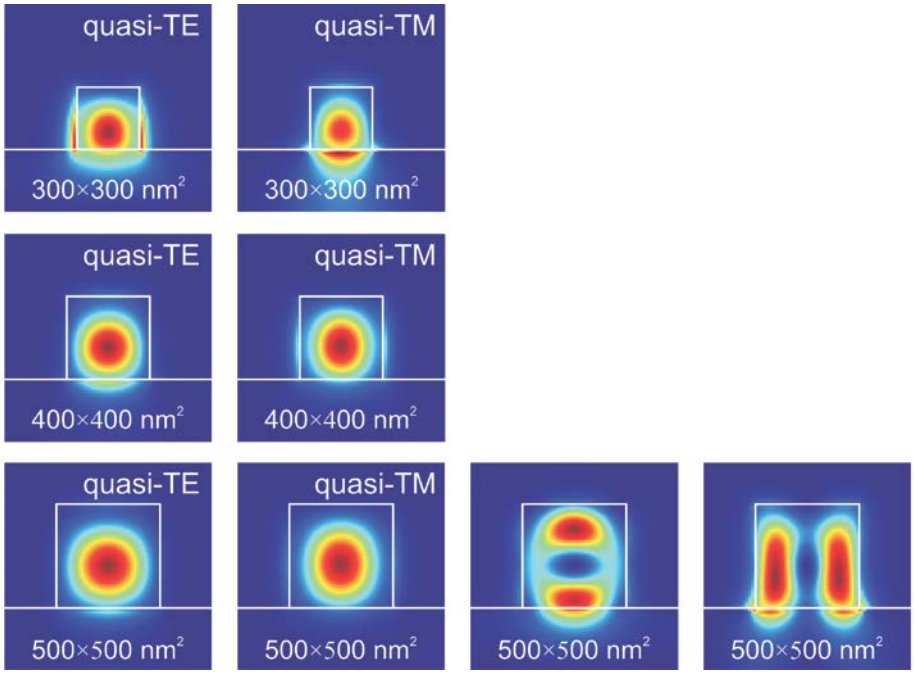

Figure S6 Field intensity profile of the modes supported by Ge waveguides on Si, for different waveguide cross sections.

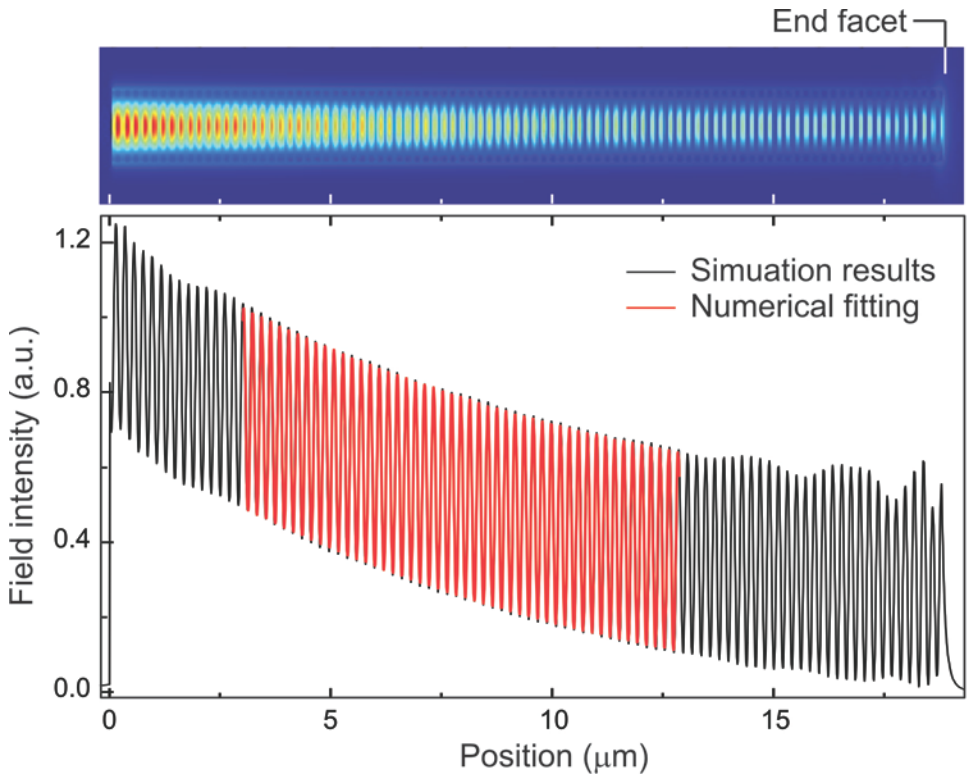

Figure S7 Simulation results and numerical fitting of a semi-infinte truncated Ge waveguide, in order to evaluate the end-facet reflectivity.

7) Simulated polarization properties of emitted light

In order to evaluate the expected polarization properties of the spontaneous emission from the nanoresonators, we repeat the simulation analysis by separating the intensity collected by the objective into two contributions, related to electric fields polarized parallel ($I_{\parallel}$) and perpendicular ($I_{\perp}$) to the resonator axis. We then compute the ratio $R = \frac{I_{\perp}}{I_{\parallel}}$ to directly compare with experiments. The results of such simulation analysis are shown in Fig. S8 and show that R varies between 1 and 4.5 with an average value of about 2.5 for the cavities under investigation, revealing that no significant degree of linear polarization is expected in the experiments.

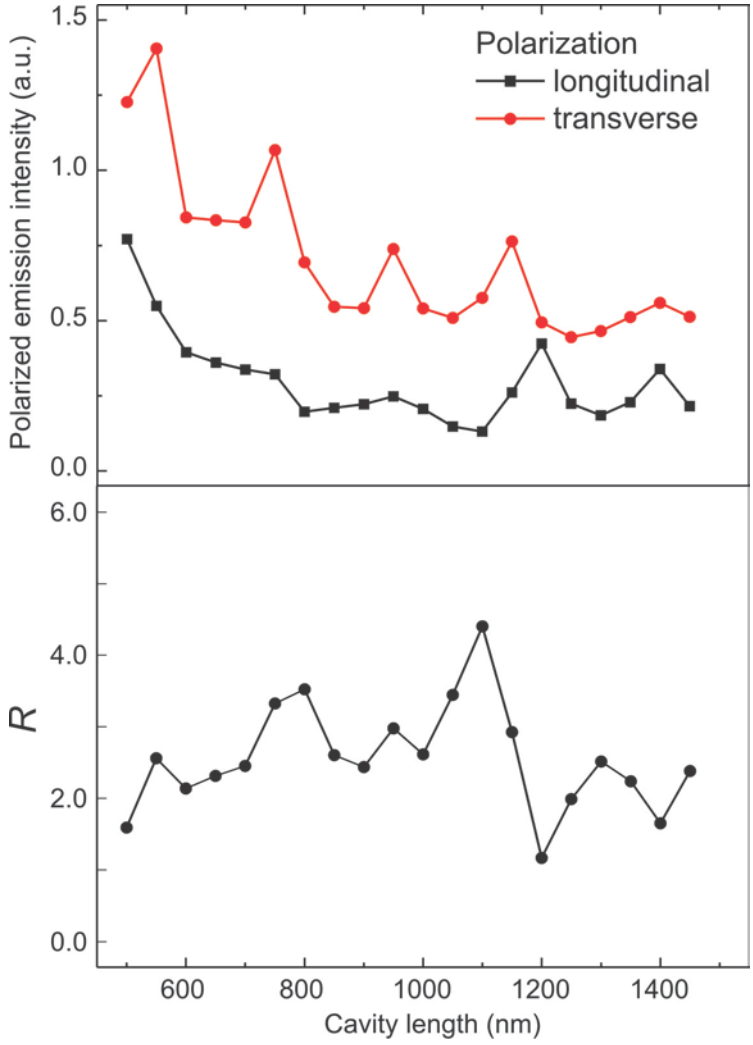

Figure S8 (a) Simulated emission intensity for photons polarized parallel ($I_{\parallel}$) or perpendicular ($I_{\perp}$) to the axis of each nanoresonator; (b) Calculated ratio $R = \frac{I_{\perp}}{I_{\parallel}}$ as a function of the length of the cavity.

8) Data analysis procedure for the experimental emission enhancement

The fluorescence maps depicted in Figure 2 in the main manuscript were collected while holding the spectrometer prism in position to select a 15 nm spectral region centered at 1550 nm in wavelength. The count rates are already corrected to account for the hold-off times of the detector and display the real number of photons impinging on the detector. To determine each antenna emission enhancement with respect to the surrounding film of germanium we have normalized the fluorescence signal with respect to the power absorbed by the illuminated Ge volume. The power by each antenna has been evaluated by analytically convoluting a Gaussian profile (FWHM = 1.3 μm) with the antenna profile.

Supplementary references

[S1] Bauer, G.; Li, J.; Koppensteiner, E. *J. Cryst. Growth* **1995**, 157, 61.

[S2] Berger, H. *X-Ray Spectrom*. **1986**, 15, 241.

[S3] Dismukes, J. P.; Ekstrom, L.; Paff, R. J. *J. Phys. Chem.* **1964**, 68, 3021.

[S4] Slack, G. A.; Bartram, S. F. *J. Appl. Phys.* **1975**, 46, 89.

[S5] Adachi, S. *Phys. Rev. B* **1988**, 38, 12966.

[S6] Lautenschlager, P.; Garriga, M.; Via, L.; Cardona, M. *Phys. Rev. B* **1987** 36, 4821.

[S7] Camacho-Aguilera, R.; Han, Z.; Cai, Y.; Kimerling, L. C.; Michel, J. *Appl. Phys. Lett.* **2013**, 102, 152106.

[S8] Öztürk, M. C.; Grider, D. T.; Wortman, J. J.; Littlejohn, M. A.; Zhong, Y.; Batchelor, D.; Russell, P. *J. Electron. Mater.* **1990**, 19, 1129.

[S9] Tosi, A.; Della Frera, A.; Bahgat Shehata, A.; Scarcella, C. *Rev. Sci. Instrum.* **2012**, 83, 013104.

[S10] Itzler, M. A.; Jiang, X. D.; Entwistle, M.; Slomkowski, K.; Tosi, A.; Acerbi, F.; Zappa, F.; Cova, S. *J. Mod. Opt.* **2011**, 58, 174.

[S11] Huang, J.-S.; Feichtner, T.; Biagioni, P.; Hecht, B. *Nano Lett.* **2009**, 9, 1897.